Doppler-shifted acoustic cyclotron resonances in beryllium

Paul M. Campbell* and Robert W. Reed
Department of Physics, The Pennsylvania State University, University Park, Pennsylvania 16802
(Received 11 April 1980)

Doppler-shifted acoustic cyclotron resonances have been observed in Be using longitudinal sound waves at frequencies up to 1.1 GHz and shear waves at frequencies up to 650 MHz. The data yield extremal derivatives of Fermi-surface cross-sectional areas. The derivative data are compared with predictions from a pseudopotential model adapted from Tripp *et al.*

INTRODUCTION

At liquid-helium temperatures, and in the presence of a magnetic field, the ultrasonic attenuation, due to the conduction electrons in a pure single-crystal metal, is known to exhibit a number of different magnetoacoustic effects. These include magnetoacoustic quantum oscillations, geometric oscillations, and Doppler-shifted acoustic cyclotron resonances (DSACR) whose inverse magnetic field periodicities are, respectively, related to extremal cross-sectional areas, extremal diameters, and extremal derivatives of cross-sectional areas of Fermi surface orbits lying in planes perpendicular to the direction of the applied magnetic field.

The present investigation is concerned with DSACR's in Be. The specimens used are the same high-purity specimens used for earlier investigations of magnetoacoustic quantum oscillations and geometric oscillations.[1-3] The present results along with the earlier magnetoacoustic studies represent a set of extensive acoustic measurements in this material. The magnetoacoustic data are in good agreement with the available de Haas–van Alphen data,[4-7] and with a parametrized pseudopotential model of the Be Fermi surface.[4]

DOPPLER-SHIFTED ACOUSTIC CYCLOTRON RESONANCES

Theories for DSACR have been developed by a number of authors.[8-11] Physically, this resonance phenomenon occurs when an electron at the Fermi surface with a drift velocity v_B along the direction of the applied magnetic field $\vec{B}$ "sees" integer multiples of the acoustic wavelength λ coincident with the pitch length of its helical orbit. Because the electron drift velocity is large compared to the sound velocity v_s, the effective sonic frequency ω_{eff} "seen" by the electrons is the sound frequency ω Doppler shifted up by the ratio of v_B/v_S. Since the sound wave propagation vector $\vec{q}$ may not lie along $\vec{B}$, the effective frequency is given by

$$\omega_{eff} = \omega(\bar{v}_B \cos\theta/v_S - 1), \tag{1}$$

where $\theta \equiv \angle \vec{q}, \vec{B}$ and $\bar{v}_B$ is the orbital time average of v_B, which is in general not constant around a cyclotron orbit for an electron in a real metal. The equation for the field values of the resonance absorption is found to be

$$\omega_{eff} = n\omega_c = neB/m_c c, \tag{2}$$

where $n = n_f - n_i$, the difference in the cyclotron quantum numbers after and before absorption of a sound phonon, is a positive integer and m_c is the effective electron mass averaged around the cyclotron orbit. For free electrons, Eq. (2) can be readily obtained by using the conservation of energy and linear momentum in the $\vec{B}$ direction for absorption of a sound phonon by a conduction electron. Equation (2) results also from a detailed analysis of the problem for a real metal.[11] Except for θ very near $\pi/2$ the "1" in Eq. (1) can be dropped since $\bar{v}_B/v_S \sim 200$. Combining Eqs. (1) and (2) yields the relation

$$\frac{1}{B} = \frac{ne\bar{v}_S}{c\omega m_c \bar{v}_B \cos\theta}, \tag{3}$$

which gives the $1/B$ values for the resonances in the ultrasonic attenuation. Now[12]

$$m_c \bar{v}_B = \frac{\hbar}{2\pi}\left|\frac{\partial A_\perp(k_B)}{\partial k_B}\right| \equiv \hbar R, \tag{4}$$

where $A_\perp(k_B)$ is the cross-sectional area of the Fermi surface perpendicular to $\vec{B}$ and containing the end point of the vector $k_B \hat{B}$.

Equation (3) now becomes

$$\frac{1}{B} = \frac{nev_S}{\hbar c\omega R \cos\theta}, \tag{5}$$

which shows that the expected resonances are periodic in $1/B$. For any given value of $1/B$, one would expect that a typical Fermi surface would have a continuum of combinations of n and R which could at the same time be resonant, and would

thereby lead to a general lack of structure in the ultrasonic attenuation as a function of B. However, as is the case for the other magnetoacoustic effects, the absorption spectrum will be dominated by regions of the Fermi-surface topology where a large electronic density of states exists along with a relatively wide band on the Fermi surface of R values of nearly the same value. Three kinds of orbits[13] may lead to DSACR's: (1) inflection-point orbits, where $|\partial A/\partial k_z|$ is a maximum and A is finite, (2) constant-slope orbits where $|\partial A/\partial k_z|$ is constant over a wide range but is not a maximum, and (3) limiting-point orbits, where $|\partial A|\partial k_z|$ is a maximum but where A tends to zero. In this investigation only type (1) orbits were observed. The type (2) orbits generally will not be observable unless the active zone is particularly wide. The type (3) orbits are expected to produce a single absorption edge rather than a series as predicted by Eq. (5).

In general, for a real metal, there are two possible electron-phonon coupling mechanisms which contribute to the acoustic attenuation. These are the deformation potential coupling and the electric field coupling.[11] The first of these can lead to resonances in the absorption of sound for both longitudinal and shear waves, with the amplitude of the resonances dependent on crystal symmetry and the sound propagation (and polarization) directions. The electric field coupling is only effective for shear waves since only these lattice distortions lead to the creation of an electric field which can exert a force on the electrons. This coupling mechanism can be evaluated through use of the conductivity tensor[11] and is expected to lead to antiresonances (i.e., minima in the attenuation) instead of resonances. In Be, which is a compensated metal, this effect is expected to be small and no antiresonances were observed in this investigation.

A necessary requirement for observation of DSACR's is that the product ql exceed 1, where l is the electron mean free path and q is the sound wave vector. This condition requires the use of very pure metal single crystals along with very high sound frequencies.

EXPERIMENTAL APPARATUS AND PROCEDURES

Most of the experimental apparatus has been described earlier.[1,14,15] The experimental conditions were very similar to those used for our earlier work on geometric oscillations in Be (Ref. 1); briefly: (1) sonic frequencies from 0.5 to 1.5 GHz were employed, (2) magnetic fields from 0 to 30 kOe were used, (3) specimen temperatures were typically 1.0 K and (4) a field-modulation technique was employed to take electronically the field derivatives of the attenuation versus $1/H$ data.

The longitudinal sound waves were generated with ZnO thin-film transducers. The shear waves were generated by use of ac-cut quartz transducers operated at odd harmonics and polarized carefully with respect to the crystalline axes. The shear frequencies were generally limited to less than 0.7 GHz, but because of the appreciably lower shear sound velocities the ql product was as high as that for the somewhat higher-frequency longitudinal sound.

The data were digitally recorded on punched paper tape. The actual recorded values were proportional to H (in oersteds), whereas the appropriate parameter is in fact B which is internal to the specimens. It was assumed that H (oersted) $= B$ (gauss) (i.e., $\mu = 1$), in the data analysis.

The digital data typically contained hundreds of sampled points per DSACR period. The data were used to generate large (40×80 cm) computer plots of both the relative changes in the attenuation, α, vs $1/H$ curves and the derivative $d\alpha/d(1/H)$ curves. Example derivative data are shown in Fig. 1. These data were carefully reduced by hand measurement, and the location of each peak was plotted versus its $1/H$ location. The slope of this plot was computed by a least-squares method, and the frequency of the oscillations (in H) was computed from this result. The associated errors for the frequency of these data were computed using the 95% confidence level interval of the fit. In some instances two DSACR frequencies were identified on a single data curve.

The data were also processed by the method of fast Fourier analysis. Because of slow background variations in the signals and the relatively low number of data points, this method produced

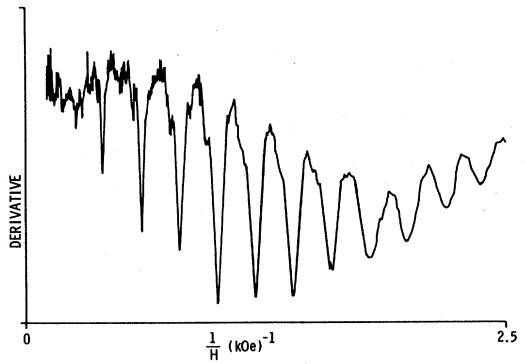

FIG. 1. Example $d\alpha/d(1/H)$ data. The oscillations result from the magnetic field derivative of a series of DSACR's. The ultrasonic frequency is 1104 MHz.

better results if the data were fitted to a third- or fourth-order polynomial with the result subtracted from each data point to eliminate background drift problems. A cosine taper was applied to the first and last 2% of the data points of a $1/H$ sweep to eliminate the side lobes usually associated with Fourier analysis of a rather limited number of oscillations. Typically only the derivative data led to useful Fourier spectrograms. The DSACR frequency determined in this way had an associated uncertainty, as taken from the 90% half-width of the peaks, on the order of a few percent.

The results of both methods of analysis were typically in full agreement and the Fourier analysis often aided in identifying multiple DSACR frequencies in the graphical method.

THE BERYLLIUM FERMI SURFACE

Figure 2 shows the Fermi surface of Be along with the first Brillouin zone. It consists of a large hole surface called the coronet, located in the second zone, and six equivalent third zone, electron surfaces which yield two "cigars" per coronet. Of the several theoretical models of the Fermi surface,[4,16-18] the semiempirical nonlocal pseudopotential model of Tripp, Everett, Gordon, and Stark[4] (TEGS) gives the best agreement with the body of available data.

No calculations of extremal area derivatives of the Be Fermi surface were available for comparison to the experimental results of the present study. John Tripp of TEGS[4] kindly supplied a copy of the computer subroutines used to generate the Be Fermi surface from the pseudopotential model presented in the TEGS paper.[4] Since that model was parametrized, using de Haas–van Alphen data as a basis for comparison, it is not surprising that the accuracy of the model in predicting extremal areas of cross section is very good.[1,3,4] However, this is no guarantee that the extremal derivatives of the cross-sectional areas are equally well predicted since they will in general not lie in the vicinity of the extremal areas where the model is known to be reliable. Hence the present experimental results are a more stringent test of the TEGS pseudopotential model.

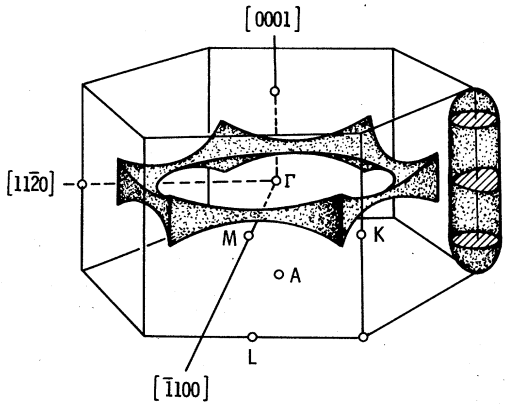

FIG. 2. Fermi surface of Be in the first Brillouin zone.

The TEGS pseudopotential model is capable of computing the cross-sectional area of any part of the Fermi surface if appropriate descriptive parameters of the plane of interest are provided. A reference Cartesian coordinate system is established with the origin at the center of the first Brillouin zone with the x axis along the $[11\bar{2}0]$ direction, the y axis along the $[10\bar{1}0]$ direction, and the z axis along the [0001] direction. The location of the plane, in which a cross-sectional area is to be calculated, is specified by the location of the origin of a planar (xy) coordinate system in terms of the location of this point with respect to the reference frame and the Euler angles ϕ and θ defining the orientation of the new planar coordinate system relative to the reference system.

In order to calculate the extremal area derivatives, a number of planes (typically 10) all perpendicular to a specified $\vec{H}$ direction and equally spaced along this direction are specified as indicated above. Cross-sectional areas of the Fermi surface are computed for each plane. These areas are fitted to a cubic spline function in k_z (the $\vec{H}$ direction). The derivative $\partial A/\partial k_z$ is evaluated in the range of the spline function. The second derivative $\partial^2 A/\partial k_z^2$ is also evaluated and a search for a zero in $\partial^2 A/\partial k_z^2$ is made. When a zero in the second derivative is found, the value of $|\partial A/\partial k_z|_{\max}$ is evaluated. Since the accuracy of this method depends on the mesh of planes originally used, a second much finer mesh is always employed for the region in k_z where the extremum was first predicted. Further refinements in this mesh were found to lead to insignificant improvements in the calculated extremal area derivatives. It is observed that this process is orders of magnitude more demanding of computer time than that for finding extremal areas.

EXPERIMENTAL RESULTS AND COMPARISON TO THE MODEL PREDICTIONS

It has been noted that the data analysis leads to values of the DSACR frequency in units of H. Then using Eq. (5) these frequencies are converted to values of $R_{\max}$:

$$R_{\max} = \frac{ev_S\bar{H}}{chf\cos\theta},$$

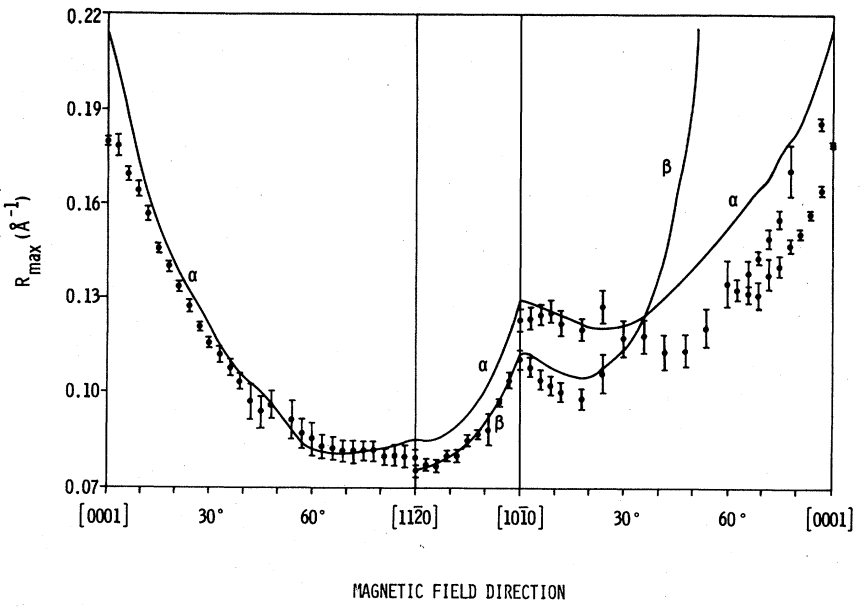

FIG. 3. Experimental and theoretical values of extremal area derivatives, R_{max}, for the coronet portions of the Be Fermi surface.

where $\overline{H}$ represents the DSACR frequency in oersteds and $f = \omega/2\pi$ is the ultrasonic frequency. The experimentally determined values for $\overline{H}$, f, and θ are the major source of errors in the experiment. The ultrasonic frequency was determined with an accuracy of ± 1 MHz, and θ was determined to within ~± 0.5°. The most significant error is associated with the determination of $\overline{H}$ and was computed as previously indicated. A composite uncertainty was computed for each data point as a function of Δf, $\Delta\theta$, and $\Delta\overline{H}$. The values used for v_S were calculated from data given by Testardi and Condon.[7]

Figure 3 is a composite plot of all of the data which are associated with DSACR's on the coronet portion of the Be Fermi surface. The solid lines were calculated using the TEGS pseudopotential model in the manner described above. The calculated curves represent all the extremal area derivatives found on the coronet. Table I gives selected experimental and theoretical R_{max} values for the curves shown in Fig. 3.

$\overline{H}$ in (10$\bar{1}$0) plane, coronet orbits

The experimental values of R_{max} in the (10$\bar{1}$0) plane are in reasonably good agreement with the calculated values represented by the curve labeled α. For $\vec{H}$ near the [0001] axis the values are about 15% lower than those predicted. However,

TABLE I. Selected experimental and theoretical R_{max} values. (The angle directions correspond to those in Fig. 3.)

Plane	$\vec{H}$ direction	Orbit designation	Experimental R_{max} (Å^{-1})	Experimental Uncertainty	Theoretical R_{max} (Å^{-1})
(10$\bar{1}$0)	[0001]	α	0.179	±0.001	0.2156
	30°	α	0.116	±0.0016	0.1206
	60°	α	0.085	±0.004	0.0822
	[11$\bar{2}$0]	α	0.079	±0.0027	0.0854
(0001)	[11$\bar{2}$0]	β	0.075	±0.0022	0.0755
	[11$\bar{2}$0]	γ	0.344	±0.0054	0.3690
	[10$\bar{1}$0]	γ	0.493	±0.0051	0.5166
	[10$\bar{1}$0]	β	0.112	±0.0021	0.1128
	[10$\bar{1}$0]	α	0.123	±0.0036	0.1298
(11$\bar{2}$0)	30°	α	0.118	±0.006	0.1218
	60°	α	0.135	±0.007	0.1530

for $\vec{H}$ more than 10° away from the [0001] direction the agreement is good. The data from 0° to 50° were taken with the sound propagating along the [0001] direction. In this case the sound was longitudinal and the frequency was 1104 MHz. No oscillations were observed with shear waves for $\vec{q} \parallel [0001]$.

For the data from 50° to 90°, the specimen used has $\vec{q} \parallel [11\bar{2}0]$. In this case only shear waves polarized along the $[10\bar{1}0]$ direction gave observable DSACR's. Since the data taken with the two specimens and with differently polarized sound waves match well, it is apparent that they came from the same branch of R_{max} values. The α branch from the coronet is the only branch located which can be identified with the data in this plane.

Figure 4 shows a sextant of the coronet as seen by looking down the [0001] axis toward the basal plane. The plane in which $\vec{H}$ lies for the α orbits is shown (edge on) by the dashed line labeled "cut 1." Figure 5 shows the shape of this $(10\bar{1}0)$ plane that cuts through the coronet lobe. The lines through this cut represent the planes in which lie the DSACR contributing orbits. These planes are perpendicular to the plane of the figure. ($\vec{H}$ lies in the plane of the figure.) For example, the 0° line represents the plane containing the orbit which has an R_{max} value for $\vec{H}$ along the [0001] direction, whereas the 90° line is for the case with $\vec{H}$ along the $[11\bar{2}0]$ direction. The path taken by electrons on the 0° α orbit is shown in Fig. 4. Note that these planes in general do not coincide with planes containing extremal cross-sectional areas. It is believed that the differences in the deformation potential for $\vec{q} \parallel [0001]$ and $\vec{q} \parallel [11\bar{2}0]$ account for the DSACR sensitivity to longitudinal sound in the first case and shear with $\vec{\epsilon} \parallel [10\bar{1}0]$ in the second case.

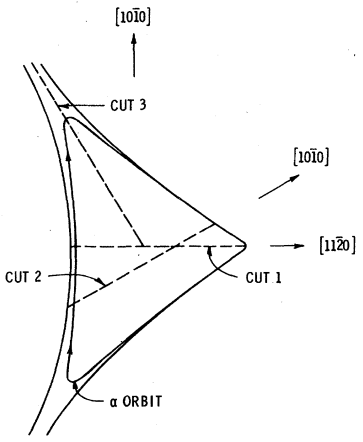

FIG. 4. Sextant of the coronet. This view is looking down the [0001] axis toward the basal plane.

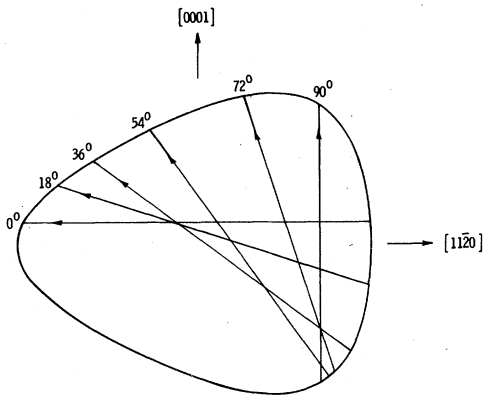

FIG. 5. Shape of a $(10\bar{1}0)$ plane through a coronet lobe. The edge of this plane is seen as cut 1 in Fig. 4. The lines in this plane represent the edge of the planes in which lie the α DSACR orbits whose R_{max} values are plotted between [0001] and $[11\bar{2}0]$ in Fig. 3.

$\vec{H}$ in (0001) plane, coronet orbits

The experimental values of R_{max} in the (0001) plane are plotted in Fig. 3 along with the theoretical values for two different sets of orbits which yield R_{max} values. The data shown were all obtained with the specimen cut so that $\vec{q} \parallel [10\bar{1}0]$. In this case only longitudinal sound resulted in observable DSACR's and a frequency of 1028 MHz was used. Because of the six-fold symmetry in the basal plane the data are unique for only a 30° range. Additional data were taken for 30° to 60° with the results being essentially identical to those shown here. The resulting R_{max} values are in complete agreement with the theoretical values for the β orbits.

Figure 6 is a top view of the coronet looking down the [0001] direction. For the β orbits shown, $\vec{H}$ (for the 0° cut) is along the $[11\bar{2}0]$ axis near the top of the figure. This will be the case for a third of the coronet lobes. The lines shown represent the cuts (perpendicular to the plane of the figure) which yield R_{max} values for $\vec{H} \parallel [11\bar{2}0]$ to $\vec{H} \parallel [10\bar{1}0]$.

The α orbits shown in Fig. 6 occur simultaneously with the β orbits but in a different pair of coronet lobes where $\vec{H}$ is taken along the $[11\bar{2}0]$ direction pointing to the left. The cut for 0° ($\vec{H} \parallel [11\bar{2}0]$) is the same as the cut labeled 90° in Fig. 5 but viewed from a perspective rotated by 90°.

The apparent good agreement of the experimental R_{max} values with those calculated for the β orbits and the lack of any data that can be attributed to the α orbits in the (0001) plane leads one to question the assignment of the data in the $(10\bar{1}0)$ plane, for $\vec{H}$ close to $[11\bar{2}0]$, to the α orbits. However, a reinvestigation of the pseudopotential model results for the $(10\bar{1}0)$ plane yielded no evidence of

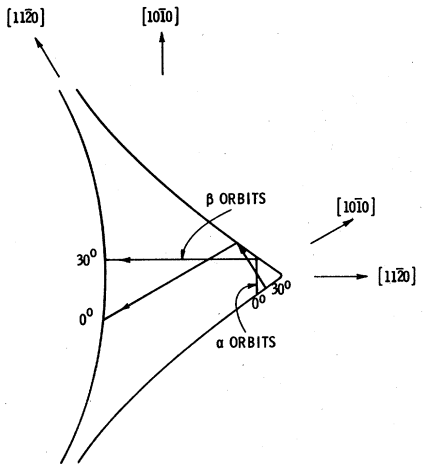

FIG. 6. Sextant of the coronet. The lines show the edge of planes in which lie the α and β orbits whose R_{max} values are plotted between [11$\bar{2}$0] and [10$\bar{1}$0] in Fig. 3. $\vec{H}$ lies in the basal plane for these orbits.

β orbits in this plane, not even for angles near the [11$\bar{2}$0] direction.

$\vec{H}$ in (11$\bar{2}$0) plane, coronet orbits

For $\vec{H}$ in the (11$\bar{2}$0) plane the data were taken using the specimens with $\vec{q} \parallel [10\bar{1}0]$ and $\vec{q} \parallel [0001]$. The ultrasound was longitudinal in both cases and the frequencies were, respectively, 1028 and 1102 MHz. The data from 0° to 60° were taken with the [10$\bar{1}$0] specimens and from 60° to 90° with the [0001] specimen. Data were also taken for $\theta < 60°$ with the [0001] specimen but the oscillations became progressively more weak as the angle was increased away from the [0001] axis. The data from both specimens were in full agreement in the region of overlap.

For angles from 0° to 30°, two distinct series of DSACR's were found. They are in fairly good agreement with the R_{max} values calculated for the α and β orbits. The β orbit DSACR's were typically stronger than the α DSACR's in this region. It is not surprising that the β data disappear at higher angles since the model calculations show rapidly increasing R_{max} values for the β orbits for $\theta > 30°$. For such orbits, it would be expected that the relative density of electron states would be small, thereby yielding low-amplitude DSACR's.

For $\theta \gtrsim 30°$ the data have an angular dependence similar to that predicted for the α orbits, but the R_{max} values are somewhat below those calculated. Furthermore, for $60° < \theta < 90°$ there were definitely two distinct DSACR frequencies. No amount of searching with the pseudopotential model gives any explanation for this double set of frequencies.

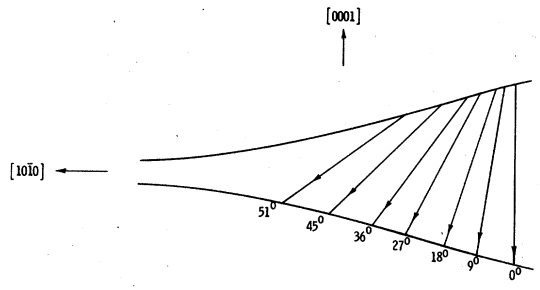

FIG. 7. Location of β orbits on the coronet for $\vec{H}$ between [10$\bar{1}$0] and [0001] in Fig. 3. The upper edge of this plane is cut 3 in Fig. 4.

Rechecks of the specimen orientation also give no explanation for these data.

Figures 7 and 8 show the location of the β and α orbits on the coronet. The upper edge of the plane shown in Fig. 7 is indicated by cut 3 in Fig. 4 while the upper edge of the plane shown in Fig. 8 corresponds to cut 2 in Fig. 4.

$\vec{H}$ in (0001) plane, cigar orbits

Figure 9 shows the only data obtained for orbits attributed to the cigar. These data, taken with the specimen having $\vec{q} \parallel [10\bar{1}0]$, were obtained at the same time as data in the (0001) plane shown in Fig. 3. The cigar data were of a substantially higher DSACR frequency and have the same general dependence on angle as that calculated for the γ orbits. The measured values for the γ orbits are consistently 5% to 7% lower than the calculated values. These data and calculated values were the only ones found for the cigar.

Figure 10 is a cross-sectional view of the cigar in the basal plane looking from the top along the [0001] direction. The cuts shown yield the R_{max} values shown in Fig. 9. The orbits on which

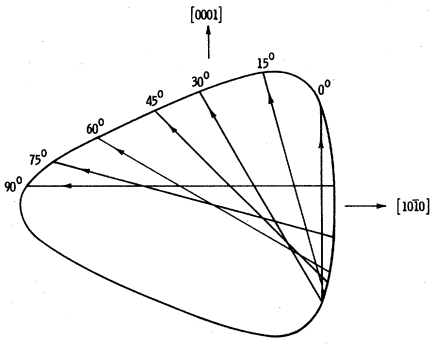

FIG. 8. Location of α orbits on the coronet for $\vec{H}$ between [10$\bar{1}$0] and [0001] in Fig. 3. The upper edge of this plane is cut 2 in Fig. 4.

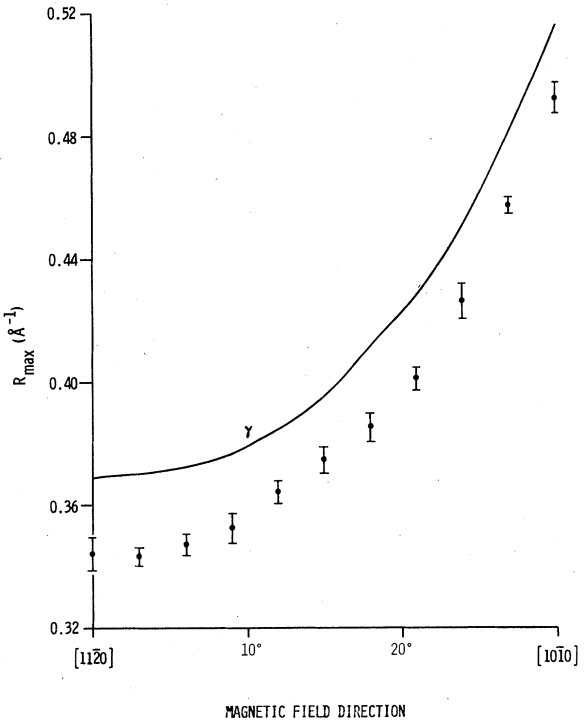

FIG. 9. Experimental and theoretical values of extremal area derivatives, R_{max}, for the cigar.

the electrons travel extend around the entire length of the cigar.

Discrepancies between theory and experiment

The major discrepancy between the theory and experiment for R_{max} values on the coronet occurs for $\vec{H}$ nearly along the [0001] direction. As an example, consider the case for the α orbits in the (1010) plane. For $\vec{H} \| [1\,1\bar{2}0]$ the orbit for R_{max} is the one labeled as 90° in Fig. 5. The shape of this orbit, which lies in a (11$\bar{2}$0) plane, is a simple oval. In this case the agreement between the theoretical

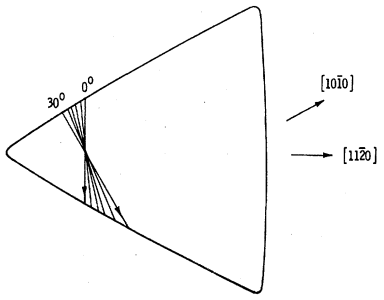

FIG. 10. Cigar cross section in the basal plane. The lines indicate the edge of planes in which lie the γ orbits whose R_{max} values are plotted in Fig. 9. $\vec{H}$ lies in the basal plane for these orbits.

and experimental R_{max} value is good. On the other hand, for $\vec{H} \| [0001]$, the orbit for R_{max} is the one labeled 0° in Fig. 5. The orbit lies in a (0001) plane and has the shape of the α orbit indicated in Fig. 4. This orbit is nearly triangular in shape and extends over a large fraction of an entire sextant of the coronet.

It is important to recall that the calculated values of R_{max} are derived from a pseudopotential model[4] in which the fundamental parameters were fit to extremal cross-sectional areas derived from de Haas–van Alphen data. Hence it is expected that the model gives its best description for orbits near these extremal areas. For the orbit shown in Fig. 4, which has here been labeled α, the orbit is rather close to the extremal area labeled as β_1^1 in the TEGS paper.[4] In the case of the α orbit shown in Fig. 4, there are no such extremal area orbits nearby. A similar situation occurs for the R_{max} values labeled γ on the cigar. There are no extremal area orbits used in the TEGS fit located in the vicinity of the γ orbits.

It is seen that the pseudopotential model gives R_{max} values in best agreement with the data when the orbits involved are in the vicinity of extremal area orbits used in the TEGS fit. (These two kinds of orbits cannot coexist in the same plane, but they can coexist in close proximity.) As the R_{max} orbits move farther away from the fitted regions, the deviations between experiment and theory grow. In any case, the deviations are not unexpectedly large and the pseudopotential model on the whole gives rather good agreement between experiment and theory.

SUMMARY

DSACR data were recorded with pure Be specimens at sonic frequencies up to 1.1 GHz. The resulting extremal derivatives of the cross-sectional areas of the Be Fermi surface were compared to those calculated using the Tripp, Everett, Gordon, and Stark[4] pseudopotential model. The experimental data were typically in agreement with the theoretical values to better than 15%. The present results show that the pseudopotential model does not yield as good agreement with DSACR data as it does with data derived from de Haas–van Alphen[4] or magnetoacoustic quantum oscillations[2,3] which predict extremal cross-sectional areas. In these latter cases, the agreement is essentially within the experimental error.

ACKNOWLEDGMENTS

The authors are particularly indebted to Dr. John Tripp of Case Western Reserve University, Cleveland, Ohio, who generously supplied and explained a duplicate of the computer routine which

computes cross-sectional areas of the Be Fermi surface from the TEGS pseudopotential model.[4] Dr. Louis R. Testardi of the Bell Telephone Laboratories, Murray Hill, New Jersey, also generously loaned a pure Be specimen which was used to verify the results presented here. Unfortunately, the very large size of that specimen prevented the use of GHz-frequency longitudinal sound waves, and only a limited number of DSACR's were seen at the lower ~400-MHz sound frequencies used. Hence the accuracy of those data was somewhat less than that presented here.

---

*Present address: General Electric Company, Schenectady, New York.

[1]E. F. Vozenilek and R. W. Reed, Phys. Rev. B 12, 1140 (1975).
[2]R. W. Reed and E. F. Vozenilek, Phys. Rev. B 13, 3320 (1976).
[3]R. W. Reed, Phys. Rev. B 15, 2416 (1977).
[4]J. H. Tripp, P. M. Everett, W. L. Gordon, and R. W. Stark, Phys. Rev. 180, 669 (1969).
[5]J. H. Condon, Phys. Rev. 145, 526 (1966).
[6]B. R. Watts, Proc. R. Soc. London A282, 521 (1964).
[7]L. R. Testardi and J. H. Condon, Phys. Rev. B 1, 3928 (1970).
[8]G. L. Kotkin, Zh. Eksp. Teor. Fiz. 41, 26 (1961) [Sov. Phys.—JETP 14, 201 (1962)].
[9]E. A. Kaner, Zh. Eksp. Teor. Fiz. 43, 216 (1962) [Sov. Phys.—JETP 16, 154 (1963)].
[10]S. G. Eckstein, Phys. Rev. Lett. 16, 611 (1966).
[11]J. Mertsching, Phys. Status Solidi 37, 465 (1970).
[12]W. A. Harrison, Phys. Rev. 118, 1190 (1960).
[13]S. W. Hui and J. A. Rayne, J. Phys. Chem. Solids 33, 611 (1972).
[14]R. W. Reed, D. E. Binnie, and F. G. Brickwedde, J. Acoust. Soc. Am. 51, 910 (1972).
[15]R. W. Reed, J. Acoust. Soc. Am. 56, 886 (1974).
[16]T. L. Loucks and P. H. Cutler, Phys. Rev. 133, A819 (1964).
[17]T. L. Loucks, Phys. Rev. 134, A1618 (1964).
[18]J. H. Terrell, Phys. Rev. 149, 526 (1966).